ACS APPLIED ENERGY MATERIALS
Cite This: ACS Appl. Energy Mater. 2019, 2, 1266−1273
Article
www.acsaem.org

Amorphous Al_2O_3 with N-Doped Porous Carbon as Efficient Polysulfide Barrier in Li−S Batteries

Shenzhen Deng,[†] Yingchun Yan,[†] Liangqin Wei,[†] Tao Li,[‡] Xin Su,[†] Xiujie Yang,[†] Zhongtao Li,*[,†] and Mingbo Wu*[,†]

[†]State Key Laboratory of Heavy Oil Processing, School of Chemical Engineering, China University of Petroleum, Qingdao 266580, China

[‡]Yankuang National Engineering Research Center of Coal Slurry Gasification and Coal Chemical Industry Co., Zaozhuang 277500, China

Supporting Information

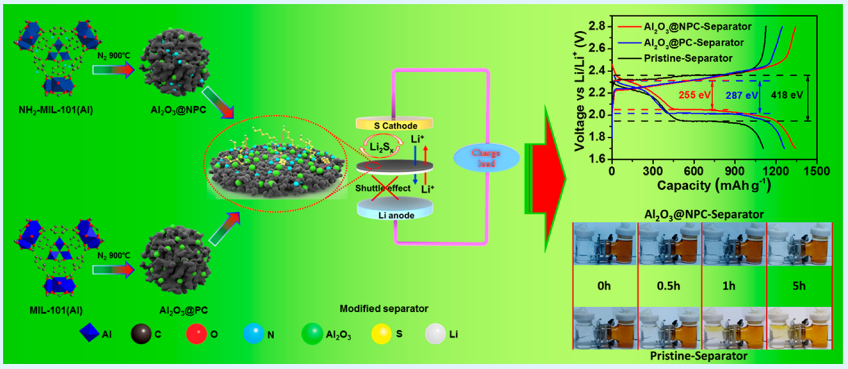

ABSTRACT: Inhibiting the shuttle effect of polysulfides is one key factor to develop a practically applicable Li−S battery. To overcome the shuttle effect, we developed here an ultrastable Li−S battery with amorphous Al_2O_3 nanohybrid separator for the first time. Through molecular design of the ligands, the material of the separator from carbonized MOF−Al at elevated temperature is composed of amorphous Al_2O_3 and N-doped porous carbon, which shows higher electrical conductivity, faster lithium diffusion and charge transfer capability, and stronger interaction with lithium polysulfides through the synergistic effect (MOF, metal−organic framework). The fabricated Li−S battery proposed here corresponds to the lowest capacity decay (only 0.054% of capacity decay in each cycle) as far as we know, which may open up new avenues for developing the next-generation lithium-ion battery.

KEYWORDS: *NH_2-MIL-101(Al), amorphous Al_2O_3, modified separator, shuttle effect, Li−S battery*

INTRODUCTION

Lithium−sulfur (Li−S) batteries are promising candidates for next-generation rechargeable batteries due to the high theoretical specific capacity (1672 mA h g^{-1}) and energy density (2600 W h kg^{-1}), which could meet the requirements of high-energy-density batteries.[1,2] Nevertheless, in the typical Li−S battery configuration, highly soluble lithium polysulfides (LiPSs) (Li_2S_n, $4 < n \leq 8$) can readily diffuse out from the cathode into the electrolyte and then shuttle between the cathode and anode during cycling, leading to capacity decay and raising the electrode resistance to limit rate performance.[3,4] Therefore, inhibiting the shuttle effect of LiPSs is one key factor to develop a practicable Li−S battery.

For the past few years, lots of strategies have been employed to enhance the electrochemical performance of the Li−S battery. Among them, combining sulfur or LiPSs within host materials including inorganic materials,[5,6] electroactive polymers,[7] carbon nanomaterials,[8−11] hybrid materials,[12] etc. is attracting increasing attention. These composites could enhance the Coulombic efficiency and improve the cycle stability as compared to that of the bare sulfur cathode. However, most host materials could not contribute any capacity, which would reduce the energy density of the Li−S battery. Thus, the cycle stability and capacity are still far from satisfactory for practical applications. Therefore, blocking PS shuttle without decreasing S content of the cathode is highly desired. Designing a separator coating through carbon materials[13] and metal derivations[14] is an effective strategy to overcome this issue, which has proven to have advantages of effective inhibition of the shuttle effect, uninfluential mass loading ratio of sulfur, and improvement of active material utilization.

Recently, amorphous materials have attracted increasing attention in energy storage fields, such as lithium-ion batteries

Received: October 22, 2018
Accepted: January 22, 2019
Published: January 22, 2019

DOI: 10.1021/acsaem.8b01815
ACS Appl. Energy Mater. 2019, 2, 1266−1273

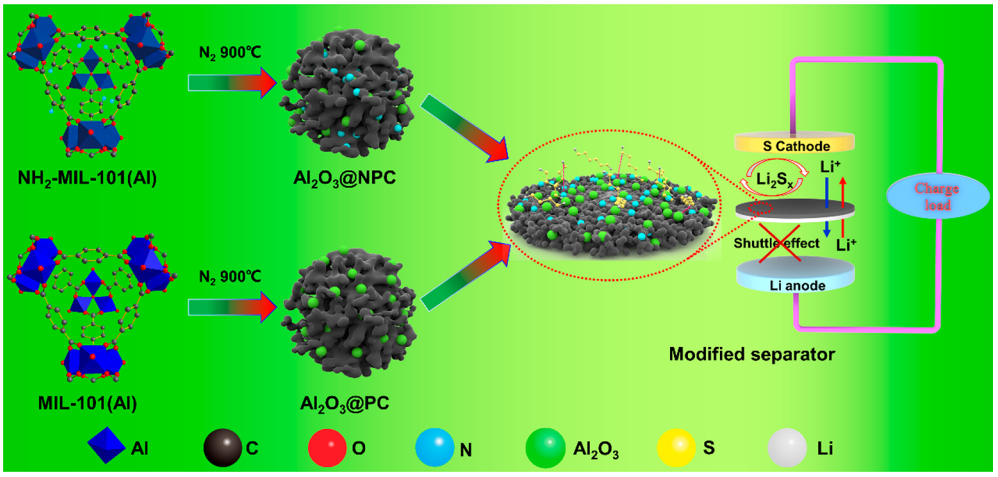

Figure 1. Preparation process of a modified separator.

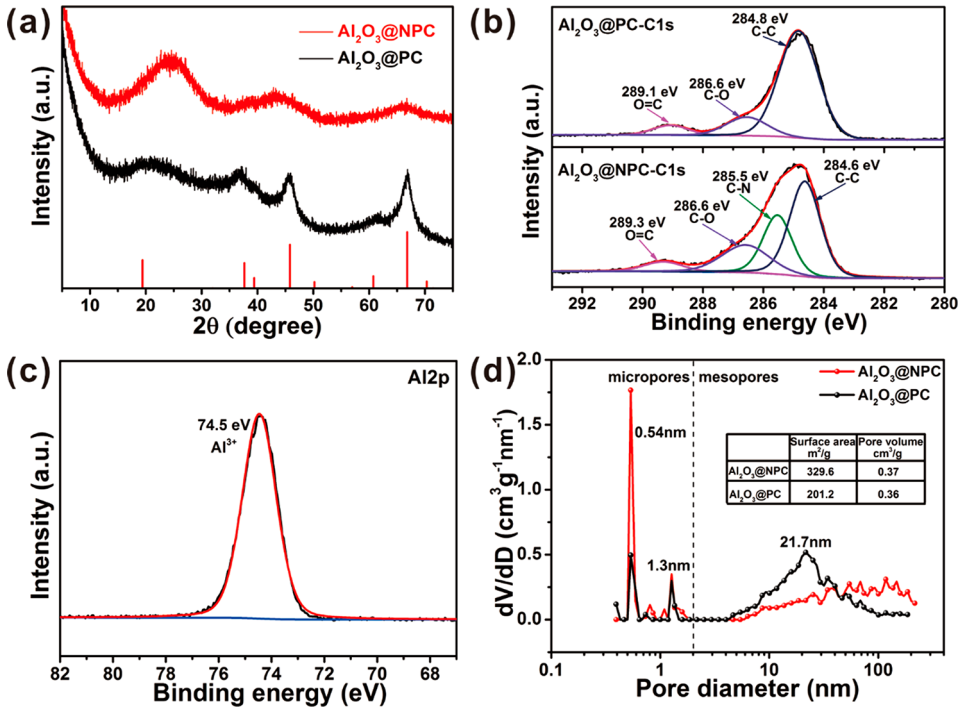

Figure 2. (a) XRD pattern and (b) C 1s XPS spectra of Al_2O_3@NPC and Al_2O_3@PC. (c) Al 2p XPS spectrum of Al_2O_3@NPC. (d) N_2 adsorption/desorption isotherms of Al_2O_3@NPC and Al_2O_3@PC.

(LIBs) and sodium-ion batteries (NIBs).[15,16] However, the application of amorphous materials as the separator in Li−S has not been reported so far. Amorphous materials could provide abundant flexible junctions to facilitate ion diffusion. Furthermore, amorphous materials possess short-range order and anisotropy that can provide more active sites for coordinating of LiPSs to overcome the shuttle effect.[17] Thus, the incorporation of the amorphous materials into the separator would significantly improve the performance of the Li−S battery. In general, amorphous materials are prepared in mild conditions, which conflict with the formation of conductive carbon at high temperature. Consequently, their design and synthesis are still an urgent problem to be solved.

The nanohybrid from the carbonized metal−organic framework (MOF) has been widely studied in many fields because of the high microporosity, large specific surface area, and uniform structures.[18,19] Therefore, adopting these materials as the separator of Li−S batteries would facilely transfer charges and ensure fast diffusion of Li^+/electrons, while the well-dispersed metal could effectively block PS shuttling through coordination interaction. Herein, two types of Al_2O_3/porous carbon nanocomposites have been successfully developed from various MOF−Al precursors to modify the separator as an efficient PS barrier (Figure 1). Through introduction of amino groups onto the ligand, the Al_2O_3@NPC exhibits the optimized structures after carbonizing at elevated temperature: uniformly distributed amorphous Al_2O_3 and porous graphitized carbon matrix. The unique structure could offer a synergistic effect on enhancing adsorption with LiPSs to overcome the side reactions that are caused by polysulfide shuttling; additionally, it could improve the compatibility and offer more open diffusion channels to accelerate lithium

DOI: 10.1021/acsaem.8b01815
ACS Appl. Energy Mater. 2019, 2, 1266−1273

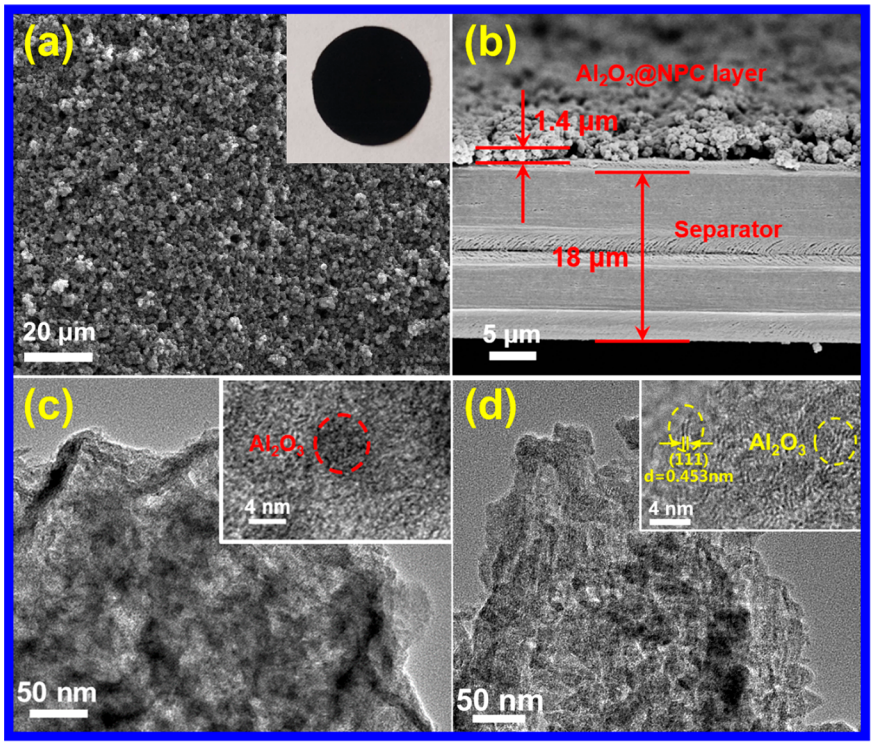

Figure 3. SEM images of the (a) surface and (b) cross-section of Al_2O_3@NPC-Separator, and the inset is the corresponding digital picture. TEM image of (b) Al_2O_3@NPC and (c) Al_2O_3@PC.

diffusion. As a consequence, most of the PSs dissolved can be transferred back to the cathode during cycling, which leads to high sulfur utilization and improved durability.

RESULTS AND DISCUSSION

The X-ray powder diffraction (XRD) patterns of two MOF precursors show typical diffraction peaks of NH_2-MIL-101(Al) (Figure S1a) and MIL-101(Al) (Figure S1b). After carbonization, the diffraction peak of graphite in Al_2O_3@NPC is stronger than that in Al_2O_3@PC (Figure 2a), and the intensity ratio of the D to the G band of Al_2O_3@NPC (0.85) is lower than 1.13 of Al_2O_3@PC (Figure S2), which reveals that the degree of graphitization is improved through introduction of N-containing groups. The higher graphitization could increase the conductivity of the composite.[20] Additionally, the main diffraction peaks at 19.4°, 37.3°, 39.3°, 45.8°, 60.8°, and 66.8° in Al_2O_3@PC (Figure 2a) can be assigned to (111), (311), (222), (400), (511), and (440) planes of $Al_{2.144}O_{3.2}$ (JCPDS 79-1557), which implies the formation of crystalline $Al_{2.144}O_{3.2}$ produced from the decomposed aluminum and oxygen during carbonization. The diffraction peaks of Al_2O_3 become extremely low and broad in Al_2O_3@NPC, which indicates that most Al_2O_3 in Al_2O_3@NPC is amorphous. The introduction of N in the precursor increased the coordination interaction with Al, which would hinder the aggregation of Al_2O_3 during hydrocracking and lead to the amorphous structure. The contents of Al_2O_3 in composites were measured by the thermogravimetric analysis (Figure S3), which indicated 61.3 and 67.2 wt % in Al_2O_3@NPC and Al_2O_3@PC, respectively.

On the basis of X-ray photoelectron spectroscopy (XPS) spectra, the Al_2O_3@NPC is mainly composed of C, N, O, and Al, and Al_2O_3@PC is composed of C, O, and Al (Figure S4a). The contents of C, O, Al, and N in Al_2O_3@NPC and Al_2O_3@PC are shown in Figure S4b. The high-resolution spectra of C 1s for Al_2O_3@NPC in Figure 2b reveal four peaks at 284.6, 285.5, 286.6, and 289.3 eV, corresponding to C—C, C—N, C—O, and C═O, respectively. Compared with the C 1s spectrum of Al_2O_3@PC, the peak at 285.5 eV in Al_2O_3@NPC confirms the formation of the C—N bond.[21−23] In addition, the peak at 74.5 eV is assigned to the Al^{3+} oxidation state of stoichiometric Al_2O_3 (Figure 2c).[24,25] N 1s XPS spectra of Al_2O_3@NPC are shown in Figure S4c, which is composed of pyridinic N (398.4 eV), pyrrolic N (400.0 eV), and graphitic N (400.9 eV). The content of pyridinic and pyrrolic N is about 79.0%, which results in an effective chemical anchoring effect to alleviate dissolution of LiPSs and improve the redeposition process during discharge/charge.[26,27] However, the graphitic N provides its p electrons to fix the defects of the π-conjugated system for higher charge transfer ability.[28,29]

The porosity of the Al_2O_3@NPC and Al_2O_3@PC is characterized by nitrogen adsorption/desorption isotherms (Figure S5). The calculated BET equivalent surface area of Al_2O_3@NPC is 329.6 $m^2\ g^{-1}$, which is somewhat higher than that of Al_2O_3@PC (201.2 $m^2\ g^{-1}$). Al_2O_3@NPC has a much higher micropore volume (*t*-plot micropore volume: 0.115 $cm^3\ g^{-1}$) than Al_2O_3@PC (*t*-plot micropore volume: 0.051 $cm^3\ g^{-1}$), which indicates that Al_2O_3@NPC contains larger surface area and more micropores to benefit the electrolyte penetration. The pore size distribution plots of Al_2O_3@NPC and Al_2O_3@PC are calculated by DFT (Figure 2d); the average pores size of Al_2O_3@NPC is around 0.5 nm which is larger than the lithium ion but smaller than lithium polysulfide, which would prevent LiPSs from diffusing through the separator, however allowing Li^+ ions to diffuse.

The SEM and EDS elemental mapping images of Al_2O_3@NPC are shown in Figure S6. Remarkably, Al_2O_3@NPC possesses a porous structure with a rough surface, and carbon,

DOI: 10.1021/acsaem.8b01815
ACS Appl. Energy Mater. 2019, 2, 1266−1273

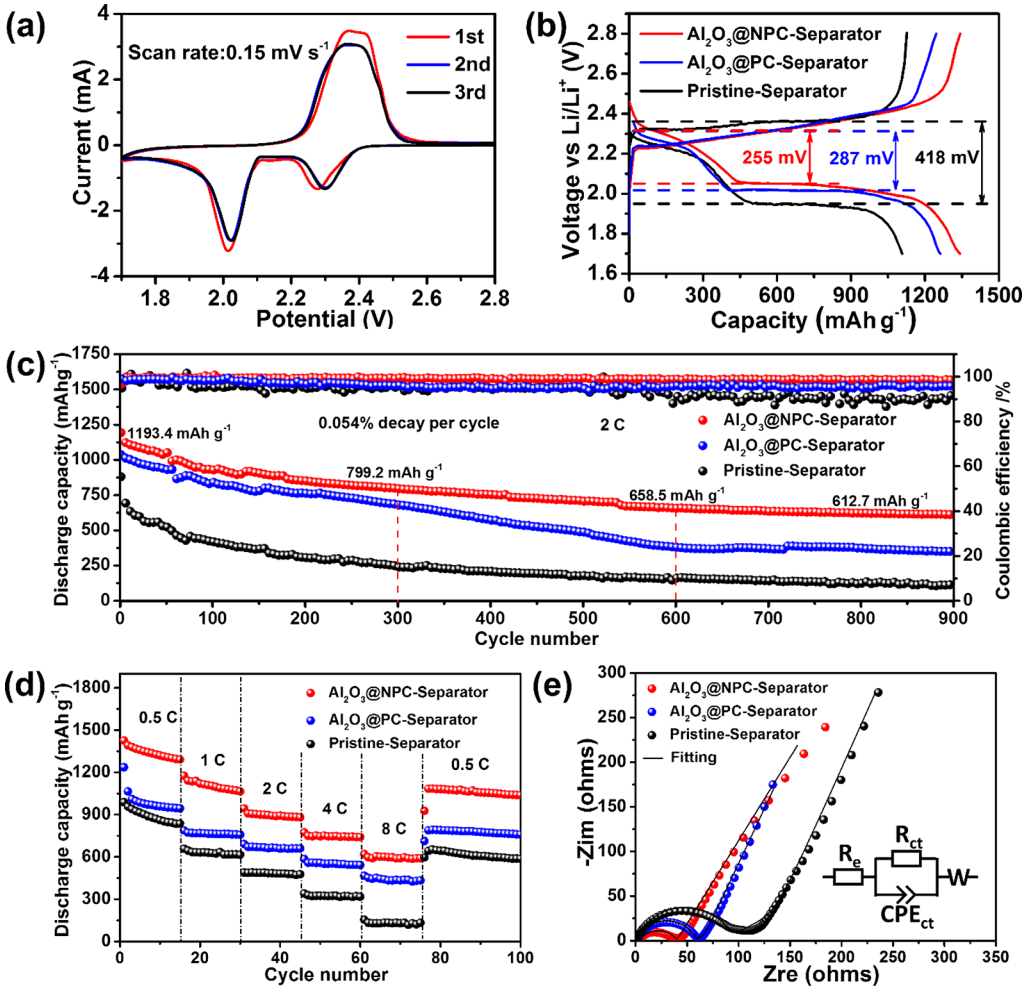

Figure 4. Electrochemical performance of cells with Al_2O_3@NPC-Separator, Al_2O_3@PC-Separator, and Pristine-Separator. (a) Cyclic voltammetry curve of cell with Al_2O_3@NPC-Separator at a sweep rate of 0.15 mV s^{-1}. (b) Calvanostatic charge−discharge curves for the first cycle at 0.5 C, and (c) long-term cycle test at 2 C. (d) Rate performance. (e) Electrochemical impedance spectra, the inset is the equivalent circuit model.

oxygen, aluminum, and nitrogen are uniformly dispersed from EDS data. The Pristine-Separator shows abundant pores on the surface (Figure S7). After coating with Al_2O_3@NPC, the nanoparticles of Al_2O_3@NPC are uniformly dispersed on the surface of the separator (Figure 3a). From the side-view SEM image in Figure 3b, the thickness of the Al_2O_3@NPC composite layer on separator is about 1.4 μm. The high-resolution TEM images of Al_2O_3@NPC and Al_2O_3@PC are given in Figure 3c,d. The lattice fringes of Al_2O_3 could not be identified in Figure 3c, which would be due to the uniform distribution and amorphous structure of Al_2O_3 in Al_2O_3@NPC. There are faint lattice fringes of Al_2O_3 crystal in Figure 3d, which suggests the formation of Al_2O_3 nanocrystals in Al_2O_3@PC, which is consistent with the result of XRD (Figure 2a).

The electrochemical properties of the Li−S batteries are studied by LIR2032 coin cells, which consist of Al_2O_3@NPC-Separator, Al_2O_3@PC-Separator, or Pristine-Separator and the sulfur−carbon black cathode with 70% S loading. While the coating weight is included in the cathode, the content of sulfur in the cathode is about 56 wt %. For the sake of contrast, the battery with Pristine-Separator is measured using the sulfur−carbon black cathode with 56% sulfur loading. Figure 4a shows cyclic voltammetry profiles of a battery with Al_2O_3@NPC-Separator for the first three cycles. The curve of each cycle exhibits repeatable two main reduction peaks and one oxidation peak. According to the electrochemical reaction, the voltage peak at about 2.30 V represents the reduction of elemental sulfur to long-chain LiPSs (Li_2S_x, $4 < x \leq 8$), and the voltage peak at about 2.05 V represents the conversion of soluble PSs to solid Li_2S_2 and Li_2S.[10,23] The CV curves of the second and third cycles are almost reduplicated with each other, which indicates highly reversible redox behavior.

The galvanostatic charge−discharge profiles of cells with the Pristine-Separator and Al_2O_3@NPC-Separator at the first cycle at 0.5 C are shown in Figure 4b. Despite the same sulfur loading, the voltage hysteresis and the length of the voltage plateaus are obviously different. The battery with Al_2O_3@NPC-Separator shows lower polarization (255 mV) than the battery with Pristine-Separator (418 mV), which represents a more kinetically efficient reaction process with a smaller barrier.[30,31] The result demonstrates that the Al_2O_3@NPC coating layer has better compatibility with the electrolyte to improve the redox reaction kinetics and the reversibility of the battery.

Figure S8 shows the cycling performances of a battery with various separators at 0.5 C. The initial discharge capacity of the battery with the Al_2O_3@NPC-Separator is 1341.9 mA h g^{-1} and still maintains at 1024.1 mA h g^{-1} after 100 cycles. The long-time cyclic performances of the battery with Pristine-

DOI: 10.1021/acsaem.8b01815
ACS Appl. Energy Mater. 2019, 2, 1266−1273

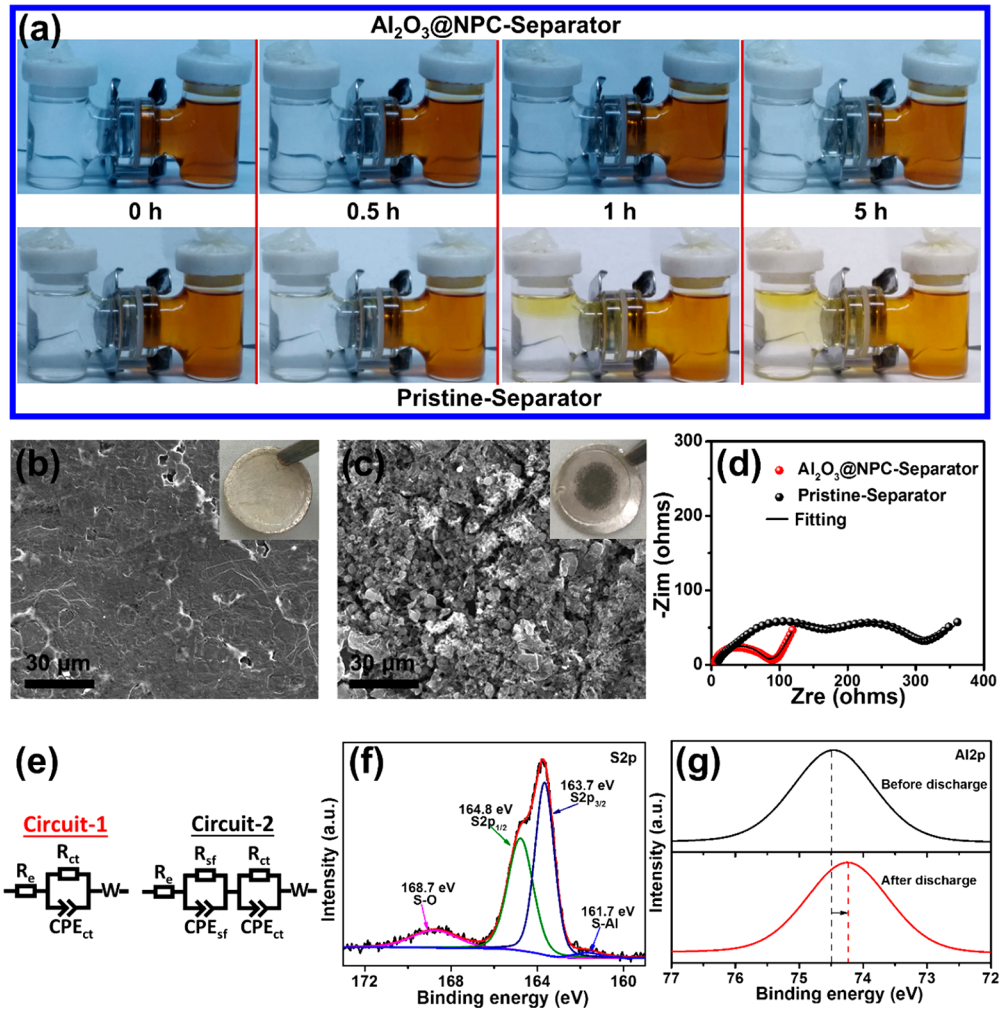

Figure 5. (a) Polysulfide permeation measurements. SEM images of the cycled lithium anode with (b) Al_2O_3@NPC-Separators and (c) Pristine-Separators, the inset is corresponding digital pictures. (d) Electrochemical impedance spectra of Li−S cells after 100 cycles, and (e) corresponding equivalent circuits. Circuit-1 stands for Al_2O_3@NPC-Separator and circuit-2 represents Pristine-Separators. (f) S 2p XPS spectra of Al_2O_3@NPC-Separator after charge−discharge. (g) Al 2p XPS spectra of Al_2O_3@NPC-Separator before and after charge−discharge.

Separator, Al_2O_3@PC-Separator, and Al_2O_3@NPC-Separator are further evaluated at a current rate of 2 C. As shown in Figure 4c (black line), the initial discharge capacity of the battery with Pristine-Separator is 880.3 mA h g^{-1}, and falls to 119.3 mA h g^{-1} after 900 cycles because of the shuttle effect of LiPSs.[32] The Al_2O_3@PC coating could improve the capacity with decaying from 1036.2 to 350.1 mA h g^{-1} after 900 cycles (blue line). The initial discharge capacity of the battery with Al_2O_3@NPC-Separator is 1193.4 mA h g^{-1}, and the capacity is still maintained at 612.7 mA h g^{-1} over 900 cycles (red line), corresponding to only 0.054% of capacity decay in each cycle, which demonstrates the most efficiency of blocking the shuttle effect of PSs.[33] The electrochemical performance of the battery with Al_2O_3@NPC-Separator is almost the best among previous excellent works involving new separators using the carbon−sulfur cathode as far as we know (Table S1).

The rate capability of cells with Al_2O_3@NPC-Separator, Al_2O_3@PC-Separator, and Pristine-Separator is investigated between 1.7 and 2.8 V. As shown in Figure 4d, the discharge capacities of the battery with Al_2O_3@NPC-Separator at 0.5, 1, 2, and 4 C after several cycles correspond to values of 1291.4, 1065.8, 881.3, and 741.1 mA h g^{-1}, respectively. Even at 8 C, the cell with Al_2O_3@NPC-Separator still presents a specific capacity of 590.7 mA h g^{-1}. When the rate reduces back to 0.5 C, a specific capacity of 1084.2 mA h g^{-1} can still be achieved, which is superior to the battery with other separators. Electrochemical impedance spectra (EIS) of the battery before cycling are shown in Figure 4e. The Nyquist plots are made up of a semicircle in the high−medium frequency region and a sloped line in the low frequency region, which are related to the charge transfer resistance (R_{ct}) and semi-infinite Warburg diffusion process, respectively.[34] The equivalent circuit models are shown in the inset. R_{ct} values of the cells with Al_2O_3@NPC-Separator, Al_2O_3@NPC-Separator, and Pristine-Separator are 35.8, 54.8, and 86.3 Ω, respectively. The smallest R_{ct} values of the cells with Al_2O_3@NPC-Separator indicate that the charge transfer resistances of cells with modified separators are obviously smaller than that of the cell with Pristine-Separator. Therefore, the conductive layer on the surface of the separator not only allows lithium-ion transmission, but also can furnish extra charge transfer paths to the electrode.

For a further demonstration of the barrier effect of Al_2O_3@NPC-Separators on lithium polysulfide, a permeation experiment of Li_2S_6 is performed using an H-shaped device shown in Figure 5a. Li_2S_6 is not able to traverse Al_2O_3@NPC-Separators within 5 h, while Li_2S_6 could easily pass through the Pristine-

DOI: 10.1021/acsaem.8b01815
ACS Appl. Energy Mater. 2019, 2, 1266−1273

Separators, which demonstrates that the Al_2O_3@NPC-Separator could avoid the diffusion of LiPSs. Figure 5b,c shows the SEM images and corresponding digital pictures of lithium anodes with Al_2O_3@NPC-Separator and Pristine-Separator after 100 cycles. The lithium anode with Pristine-Separator is coarse and generates black sediment, which is likely attributed to uniform deposition of Li_2S/Li_2S_2 on the Li anode through parasitic reactions between lithium and PSs. The dissolved PSs move to the anode and react with the Li, which results in capacity loss and poor cycle stability. In addition, the reaction of PSs with the lithium anode could form an insulated Li_2S/Li_2S_2 layer on the surface of the Li anode, which passivates the Li anode with uniform Li deposition to decrease cycle stability and rate performance. In contrast, the lithium anode with Al_2O_3@NPC-Separator is cleaner and flat, which suggests that Al_2O_3@NPC-Separator could effectively inhibit the shuttle effect. For confirmation of the shuttle-suppressing and dendrite-suppressing ability of Al_2O_3@NPC-Separators, the surface EDS elemental mapping images and elemental contents of Li anodes extracted from cells after 100 cycles at 0.5 C are displayed in Figure S9. The surface of the lithium anode from the battery with Al_2O_3@NPC-Separator has lower sulfur content, which confirms the high PS inhibition capacity of Al_2O_3@NPC-Separator.

To further value the improved battery with Al_2O_3@NPC-Separator, the electrochemical impedance spectra of the battery with Al_2O_3@NPC-Separator and Pristine-Separator after 100 cycles are carried out (Figure 5d). The equivalent circuit models are presented in Figure 5e, and the result of the impedance simulation is shown in Table 1. R_e represents

Table 1. Result of Impedance Simulation for Al_2O_3@NPC-Separator and Pristine-Separator

parameter	Pristine-Separator	Al_2O_3@NPC-Separator
R_e (Ω)	5.68	1.49
R_{sf} (Ω)	139.14	
R_{ct} (Ω)	122.10	76.58

interphase-contact resistance of the electrolyte and electrode, and R_{sf} represents surface film resistance; CPE represents the corresponding constant phase element about the double layer capacitance, and R_{ct} represents charge transfer resistance. W represents Warburg diffusion impedance.[35] Another semicircle (R_{sf}) appears for Pristine-Separator after 100 cycles, which could be due to the formation of an insulating layer on the Li anode.[14] After introduction of the Al_2O_3@NPC layer, the formation of a Li_2S_2 or Li_2S deposition layer and the surface corrosion of the Li anode are effectively suppressed, which attributes to the existence of only one semicircle. This result is in good agreement with data of polysulfide permeation experiments (Figure 5a).

For exploration of the interaction between LiPSs and Al_2O_3@NPC, XPS of Al_2O_3@NPC-Separator from a cell cycled 50 times is measured. Figure 5f shows the high-resolution spectrum of the S 2p peak. Three sulfur environments at the binding energy of 163.7, 164.8, and 168.7 eV are in keeping with S $2p_{3/2}$, S $2p_{1/2}$, and S−O.[29,36] In addition, the peak at binding energy of 161.7 eV reveals the formation of S−Al bonding,[37] which suggests that chemical binding between Al_2O_3 and polysulfide is firm even after long-time cycling. Figure 5g shows the high-resolution spectra of 2p peaks of Al before and after charge−discharge. The Al 2p peak shows a slightly negative shift from 74.5 to 74.2 eV, which also suggests the Al−S_n^{2-} interaction.[14,38,39] The XPS results confirm that the Al_2O_3@NPC layer not only could anchor LiPSs but also could furnish free spaces to accommodate all kinds of PSs intermediates. As a result, the shuttle effect of LiPSs is effectively depressed.

All in all, the amorphous Al_2O_3@NPC-Separator can notably improve the rate performance, capacity, and durability of Li−S cells through the following reasons: First, the amorphous Al_2O_3 and doped N could expose more active sites to anchor LiPSs, and prevent PSs from transferring to the Li anode, which can suppress shuttling and lithium dendrites during the cyclic process. Accordingly, the Coulombic efficiency and the utilization of active material are obviously enhanced. Second, the Al_2O_3@NPC layer has abundant open diffusion channels, which is advantageous for penetration of ions and diffusion of electrolyte. Third, the carbonization can increase the conductivity of Al_2O_3@NPC, which can improve the rate performance of the battery.

CONCLUSION

In conclusion, through modulating the chemical structure of the ligand, amorphous Al_2O_3/porous carbon nanohybrids are developed through carbonizing a MOF−Al at elevated temperature, which are adopted as the coating material on a polypropylene separator for the Li−S battery. Amorphous nanohybrids possess a uniform structure and higher surface area and rate of micropores. When the amorphous Al_2O_3@NPC-coated separator is sealed into the Li−S cell, the following advantages are achieved: (1) a synergistic effect between amorphous Al_2O_3 and N-doped porous carbon to enhance interactions with polysulfide for suppressing the shuttle effect and lithium dendrites; (2) an optimized porous structure and more open diffusion channels inside amorphous Al_2O_3 leading to superior permeation and diffusion of the electrolyte; and (3) higher electrical conductivity after carbonizing at elevated temperature with N doping, which could enhance the conductivity of the battery system and then improve rate performances of the Li−S battery. As a result, the Li−S cell with Al_2O_3@NPC-Separator delivers an optimal discharge capacity of 612.7 mA h g^{-1} at 2 C with the Coulombic efficiency of 98.5% after 900 cycles, which is the highest so far that we know. The above results indicate that this modified separator makes commercialization of the Li−S battery possible and holds significant future prospects.

ASSOCIATED CONTENT

Supporting Information

The Supporting Information is available free of charge on the ACS Publications website at DOI: 10.1021/acsaem.8b01815.

Experimental methods, XRD pattern of MOF(Al), Raman spectra, TGA curves, XPS full spectra of composites and N 1s XPS spectrum of Al_2O_3@NPC, EDS elemental mapping images, nitrogen adsorption/desorption isotherms, cycle performances of cells with various separators at 0.5 C, and comparisons of electrochemical performances of this work with previous excellent works (PDF)

AUTHOR INFORMATION

Corresponding Authors

*E-mail: liztao@upc.edu.cn.

DOI: 10.1021/acsaem.8b01815
ACS Appl. Energy Mater. 2019, 2, 1266−1273

*E-mail: wumb@upc.edu.cn (alternative email 1530629808@qq.com).

ORCID

Zhongtao Li: 0000-0003-0157-6098

Mingbo Wu: 0000-0003-0048-778X

Notes

The authors declare no competing financial interest.

■ ACKNOWLEDGMENTS

Z.L. received funding from the National Natural Science Foundation of China (Grants 21572269, 21502227, 51873231), and Fundamental Research Funds for Chinese Central Universities 17CX05015, Key Research and Development Program of Shandong Province 2017GGX40118, Scientific Research and Technology Development Project of Petrochina Co., LTD (2016B-2004(GF)). S.D. received funding from Graduate student innovation projects of China University of Petroleum (YCX2017038).

■ REFERENCES

(1) Li, Z.; Deng, S.; Xu, R.; Wei, L.; Su, X.; Wu, M. Combination of Nitrogen-Doped Graphene with MoS_2 Nanoclusters for Improved Li-S Battery Cathode: Synthetic Effect between 2D Components. *Electrochim. Acta* **2017**, *252*, 200−207.

(2) Li, F.; Kaiser, M. R.; Ma, J.; Guo, Z.; Liu, H.; Wang, J. Free-Standing Sulfur-Polypyrrole Cathode in Conjunction with Polypyrrole-Coated Separator for Flexible Li-S Batteries. *Energy Storage Mater.* **2018**, *13*, 312−322.

(3) Liu, X.; Huang, J. Q.; Zhang, Q.; Mai, L. Q. Nanostructured Metal Oxides and Sulfides for Lithium-Sulfur Batteries. *Adv. Mater.* **2017**, *29*, 1601759.

(4) Urbonaite, S.; Poux, T.; Novák, P. Progress Towards Commercially Viable Li-S Battery Cells. *Adv. Energy Mater.* **2015**, *5*, 1500118.

(5) Mao, Y. Y.; Li, G. R.; Guo, Y.; Li, Z. P.; Liang, C.; Peng, X. S.; Lin, Z. Foldable Interpenetrated Metal-Organic Frameworks/Carbon Nanotubes Thin Film for Lithium-Sulfur Batteries. *Nat. Commun.* **2017**, *8*, 14628.

(6) Park, H.; Siegel, D. J. Tuning the Adsorption of Polysulfides in Lithium-Sulfur Batteries with Metal-Organic Frameworks. *Chem. Mater.* **2017**, *29*, 4932−4939.

(7) Oschmann, B.; Park, J.; Kim, C.; Char, K.; Sung, Y. E.; Zentel, R. Copolymerization of Polythiophene and Sulfur to Improve the Electrochemical Performance in Lithium-Sulfur Batteries. *Chem. Mater.* **2015**, *27*, 7011−7017.

(8) Ding, B.; Yuan, C. Z.; Shen, L. F.; Xu, G. Y.; Nie, P.; Lai, Q. X.; Zhang, X. G. Chemically Tailoring the Nanostructure of Graphene Nanosheets to Confine Sulfur for High-Performance Lithium-Sulfur Batteries. *J. Mater. Chem. A* **2013**, *1*, 1096−1101.

(9) Ji, L. W.; Rao, M. M.; Zheng, H. M.; Zhang, L.; Li, Y. C.; Duan, W. H.; Guo, J. H.; Cairns, E. J.; Zhang, Y. G. Graphene Oxide as a Sulfur Immobilizer in High Performance Lithium/Sulfur Cells. *J. Am. Chem. Soc.* **2011**, *133*, 18522−18525.

(10) Cao, J.; Chen, C.; Zhao, Q.; Zhang, N.; Lu, Q. Q.; Wang, X. Y.; Niu, Z. Q.; Chen, J. A Flexible Nanostructured Paper of a Reduced Graphene Oxide-Sulfur Composite for High-Performance Lithium-Sulfur Batteries with Unconventional Configurations. *Adv. Mater.* **2016**, *28*, 9629−9636.

(11) Niu, Z. Q.; Zhou, W. Y.; Chen, J.; Feng, G. X.; Li, H.; Hu, Y. S.; Ma, W. J.; Dong, H. B.; Li, J. Z.; Xie, S. S. A Repeated Halving Approach to Fabricate Ultrathin Single-Walled Carbon Nanotube Films for Transparent Supercapacitors. *Small* **2013**, *9*, 518−524.

(12) Fan, Q.; Liu, W.; Weng, Z.; Sun, Y. M.; Wang, H. L. Ternary Hybrid Material for High-Performance Lithium-Sulfur Battery. *J. Am. Chem. Soc.* **2015**, *137*, 12946−12953.

(13) Chung, S. H.; Manthiram, A. Bifunctional Separator with a Light-Weight Carbon-Coating for Dynamically and Statically Stable Lithium-Sulfur Batteries. *Adv. Funct. Mater.* **2014**, *24*, 5299−5306.

(14) Ghazi, Z. A.; He, X.; Khattak, A. M.; Khan, N. A.; Liang, B.; Iqbal, A.; Wang, J. X.; Sin, H.; Li, L. S.; Tang, Z. Y. MoS_2/Celgard Separator as Efficient Polysulfide Barrier for Long-Life Lithium-Sulfur Batteries. *Adv. Mater.* **2017**, *29*, 1606817.

(15) Huang, S.; Zhang, L.; Liu, L.; Liu, L.; Li, J.; Hu, H.; Wang, J.; Ding, F.; Schmidt, O. G. Rationally Engineered Amorphous TiO_x/Si/TiO_x Nanomembrane as an Anode Material for High Energy Lithium Ion Battery. *Energy Storage Mater.* **2018**, *12*, 23−29.

(16) Lu, P.; Sun, Y.; Xiang, H.; Liang, X.; Yu, Y. 3D Amorphous Carbon with Controlled Porous and Disordered Structures as a High-Rate Anode Material for Sodium-Ion Batteries. *Adv. Energy Mater.* **2018**, *8*, 1702434.

(17) Kim, N.; Chae, S.; Ma, J.; Ko, M.; Cho, J. Fast-Charging High-Energy Lithium-Ion Batteries via Implantation of Amorphous Silicon Nanolayer in Edge-Plane Activated Graphite Anodes. *Nat. Commun.* **2017**, *8*, 812.

(18) Xu, X.; Liu, J.; Liu, J.; Ouyang, L.; Hu, R.; Wang, H.; Yang, L.; Zhu, M. A General Metal-Organic Framework (MOF)-Derived Selenidation Strategy for In Situ Carbon-Encapsulated Metal Selenides as High-Rate Anodes for Na-Ion Batteries. *Adv. Funct. Mater.* **2018**, *28*, 1707573.

(19) Chen, K.; Sun, Z.; Fang, R.; Shi, Y.; Cheng, H.-M.; Li, F. Metal−Organic Frameworks (MOFs)-Derived Nitrogen-Doped Porous Carbon Anchored on Graphene with Multifunctional Effects for Lithium−Sulfur Batteries. *Adv. Funct. Mater.* **2018**, *28*, 1707592.

(20) Chen, W.; Jiang, H.; Hu, Y. J.; Dai, Y. H.; Li, C. Z. Mesoporous Single Crystals $Li_4Ti_5O_{12}$ Grown on RGO as High-Rate Anode Materials for Lithium-Ion Batteries. *Chem. Commun.* **2014**, *50*, 8856.

(21) Lei, T. Y.; Chen, W.; Huang, J. W.; Yan, C. Y.; Sun, H. X.; Wang, C.; Zhang, W. L.; Li, Y. R.; Xiong, J. Multi-Functional Layered WS_2 Nanosheets for Enhancing the Performance of Lithium-Sulfur Batteries. *Adv. Energy Mater.* **2017**, *7*, 1601843.

(22) Luo, S. W.; Yao, M. J.; Lei, S.; Yan, P. Z.; Wei, X.; Wang, X. T.; Liu, L. L.; Niu, Z. Q. Freestanding Reduced Graphene Oxide-Sulfur Composite Films for Highly Stable Lithium-Sulfur Batteries. *Nanoscale* **2017**, *9*, 4646−4651.

(23) Hu, K.; Tao, L.; Liu, D.; Huo, J.; Wang, S. Sulfur-Doped Fe/N/C Nanosheets as Highly-Efficient Electrocatalysts for Oxygen Reduction Reaction. *ACS Appl. Mater. Interfaces* **2016**, *8*, 19379−19385.

(24) Ramos, R.; Cunge, G.; Joubert, O.; Sadeghi, N.; Mori, M.; Vallier, L. Plasma/Reactor Walls Interactions in Advanced Gate Etching Processes. *Thin Solid Films* **2007**, *515*, 4846−4852.

(25) Calderone, A.; Lazzaroni, R.; Bredas, J. L.; Le, Q. T.; Pireaux, J. J. The Aluminum/Polyethylene Terephthalate Interface: A Joint Theoretical and Experimental Study. *J. Chem. Phys.* **1995**, *102*, 4299−4307.

(26) Liu, J. H.; Li, W. F.; Duan, L. M.; Li, X.; Ji, L.; Geng, Z. B.; Huang, K. K.; Lu, L. H.; Zhou, L. S.; Liu, Z. R. A Graphene-Like Oxygenated Carbon Nitride Material for Improved Cycle-Life Lithium/Sulfur Batteries. *Nano Lett.* **2015**, *15*, 5137−5142.

(27) Qiu, Y. C.; Li, W. F.; Zhao, W.; Li, G. Z.; Hou, Y.; Liu, M. N.; Zhou, L. S.; Ye, F. M.; Li, H. F.; Wei, Z. H. High-Rate, Ultralong Cycle-Life Lithium/Sulfur Batteries Enabled by Nitrogen-Doped Graphene. *Nano Lett.* **2014**, *14*, 4821−4827.

(28) Hou, T. Z.; Chen, X.; Peng, H. J.; Huang, J. Q.; Li, B. Q.; Zhang, Q.; Li, B. Design Principles for Heteroatom-Doped Nanocarbon to Achieve Strong Anchoring of Polysulfides for Lithium-Sulfur Batteries. *Small* **2016**, *12*, 3283−3291.

(29) Wang, N. N.; Xu, Z. F.; Xu, X.; Liao, T.; Tang, B.; Bai, Z. C.; Dou, S. X. Synergistically Enhanced Interfacial Interaction to Polysulfide via N,O Dual-Doped Highly Porous Carbon Microrods for Advanced Lithium-Sulfur Batteries. *ACS Appl. Mater. Interfaces* **2018**, *10*, 13573−13580.

(30) Pei, F.; Lin, L. L.; Ou, D. H.; Zheng, Z. M.; Mo, S. G.; Fang, X. L.; Zheng, N. F. Self-Supporting Sulfur Cathodes Enabled by Two-

DOI: 10.1021/acsaem.8b01815
ACS Appl. Energy Mater. 2019, 2, 1266−1273

Dimensional Carbon Yolk-Shell Nanosheets for High-Energy-Density Lithium-Sulfur Batteries. *Nat. Commun.* **2017**, *8*, 482.
(31) Zhai, P. Y.; Huang, J. Q.; Zhu, L.; Shi, J. L.; Zhu, W. C.; Zhang, Q. Calendering of free-standing electrode for lithium-sulfur batteries with high volumetric energy density. *Carbon* **2017**, *111*, 493−501.
(32) Yoo, J.; Cho, S.-J.; Jung, G. Y.; Kim, S. H.; Choi, K.-H.; Kim, J.-H.; Lee, C. K.; Kwak, S. K.; Lee, S.-Y. COF-net on CNT-net as a molecularly designed, hierarchical porous chemical trap for polysulfides in lithium-sulfur batteries. *Nano Lett.* **2016**, *16*, 3292−3300.
(33) Pang, Q.; Nazar, L. F. Long-Life and High-Areal-Capacity Li-S Batteries Enabled by a Light-Weight Polar Host with Intrinsic Polysulfide Adsorption. *ACS Nano* **2016**, *10*, 4111−4118.
(34) Xu, G. Y.; Yan, Q. B.; Kushima, A.; Zhang, X. G.; Pan, J.; Li, J. Conductive Graphene Oxide-Polyacrylic Acid (GOPAA) Binder for Lithium-Sulfur Battery. *Nano Energy* **2017**, *31*, 568−574.
(35) Tan, L.; Li, X.; Wang, Z.; Guo, H.; Wang, J. Lightweight Reduced Graphene Oxide@MoS_2 Interlayer as Polysulfide Barrier for High-Performance Lithium-Sulfur Batteries. *ACS Appl. Mater. Interfaces* **2018**, *10*, 3707−3713.
(36) Li, J.; Huang, Y. D.; Zhang, S.; Jia, W.; Wang, X. C.; Guo, Y.; Jia, D. Z.; Wang, L. S. Decoration of Silica Nanoparticles on Polypropylene Separator for Lithium-Sulfur Batteries. *ACS Appl. Mater. Interfaces* **2017**, *9*, 7499−7504.
(37) Li, X. X.; Ding, K.; Gao, B.; Li, Q. W.; Li, Y. Y.; Fu, J. J.; Zhang, X. M.; Chu, P. K.; Huo, K. F. Freestanding Carbon Encapsulated Mesoporous Vanadium Nitride Nanowires Enable Highly Stable Sulfur Cathodes for Lithium-Sulfur Batteries by Chemical Anchoring and Physical Trapping of Polysulfides. *Nano Energy* **2017**, *40*, 655−662.
(38) Sun, J.; Sun, Y. M.; Pasta, M.; Zhou, G. M.; Li, Y. Z.; Liu, W.; Xiong, F.; Cui, Y. Entrapment of Polysulfides by a Black-Phosphorus-Modified Separator for Lithium-Sulfur Batteries. *Adv. Mater.* **2016**, *28*, 9797−9803.
(39) Shao, H. Y.; Huang, B. C.; Liu, N. Q.; Wang, W. K.; Zhang, H.; Wang, A. B.; Wang, F.; Huang, Y. Q. Modified Separators Coated with a $Ca(OH)_2$-Carbon Framework Derived from Crab Shells for Lithium-Sulfur Batteries. *J. Mater. Chem. A* **2016**, *4*, 16627−16634.

DOI: 10.1021/acsaem.8b01815
ACS Appl. Energy Mater. 2019, 2, 1266−1273